

RESEARCH ARTICLE

Improved chloride binding stability for hydration products of calcium aluminates by phosphorus modification

Jia-Ao Wang^{1,2}  | Shoude Wang¹ | Graeme Henkelman²

¹Shandong Provincial Key Laboratory of Preparation and Measurement of Building Materials, University of Jinan, Jinan, China

²Department of Chemistry and the Oden Institute for Computational Engineering and Sciences, The University of Texas at Austin, Austin, Texas, USA

Correspondence

Shoude Wang, Shandong Provincial Key Laboratory of Preparation and Measurement of Building Materials, University of Jinan, Jinan 250022, China.
Email: mse_wangsd@ujn.edu.cn

Graeme Henkelman, Department of Chemistry and the Oden Institute for Computational Engineering and Sciences, The University of Texas at Austin, Austin, TX, 78712-0165, USA.
Email: henkelman@utexas.edu

Funding information

Natural Science Foundation of China, Grant/Award Numbers: 52072149, 51672108; Taishan Scholars Program; Case-by-Case partial for Top Outstanding Talents of Jinan; Welch Foundation, Grant/Award Number: F-1841

Abstract

Improved chloride binding stability for calcium aluminate cements is proposed by the doping of phosphorus. Phosphorus-modified aluminates clinker has an improved chloride binding stability compared to pristine aluminates, ordinary Portland cement and sulfur-modified calcium aluminates, as verified by experimental observation. The existence of the newly found phosphorus-modified Friedel's salt (PFS) accounts for the excellent chloride binding stability, which was understood by density functional theory calculations. Local density of states of the valence band minimum is predominantly localized around P atoms in the PFS, but evenly distributed in the Friedel's salt (FS). The frontier band energy of the partial density of states on Cl and O elements in the PFS is lower than that in the FS by 0.21 and 0.05 eV, respectively. This makes the PFS more stable than the FS salt to ionic attack.

KEYWORDS

chloride binding stability, density functional theory, Friedel's salt, phosphorus doping

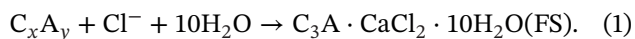
1 | INTRODUCTION

Free chloride ions play a devastating role in the corrosion of steel in offshore construction. The anti-permeation and chloride binding performance of the cement-based substrate are directly related to the corrosion of the reinforcement.^{1,2} Chloride corrosion in reinforcement can be retarded by filling with a fine mineral admixture,^{3,4} which is beneficial for growing and evolving a dense intertwined gel-like micromorphology and thereby decreasing the external chloride penetration rates. Calcium aluminate cements (CACs) is a common admixture additive in offshore construction for its chloride binding ability since it contains high aluminates. However, its chloride

binding stability is less than satisfactory and deep insight is required for guiding how to improve the chloride binding stability.

Current reports attribute the chloride binding into two mechanisms: physical binding and chemical binding. Physically bound chloride ions (such as bound by aluminum hydroxide gel⁵) are unstable and vulnerable to environmental changes. Even worse, physical binding would re-release bound Cl⁻ ions from the gel-phase to the pore fluid. Hence, admixtures with a certain chemical chloride binding ability are being increasingly considered. Ground granulated blast furnace slags (GGBFs),⁶ fly ash (FA),⁷ aluminous slag⁸ and metakaolin^{9,10} with high active aluminum-containing phases are frequently

used for chloride binding. Chloride binding is attributed to the aluminum-rich phases of aluminum-rich minerals in the admixtures such as tricalcium aluminate (C_3A), krotite (CA), grossite (CA_2), hibonite (CA_6), and mayenite ($C_{12}A_7$), which react with Cl^- directly or indirectly (by reacting with their hydration products) and form the chloride-containing phase Friedel's salt (FS),^{11–15} as shown in Equation (1):



The formation of FS as a chloride-containing phase could indeed be responsible for the superior chloride binding ability in aluminate-rich cement-based materials; however, its stability is unsatisfactory. Aluminum-rich materials are widely used for enhancing the chloride binding ability of marine structures. Nonetheless, owing to the carbonation and other multifaceted factors in the corrosive oceanic environment, the chemically bound chloride in the FS would be released to the pore solution again, subsequently leading to the inward corrosion to the steel bar when the concentration of chloride ions reach the chloride threshold value. Indeed, there are several factors which both complicate and drastically affect the stability of FS, such as ion concentration, temperature, pore solution pH, electrical fields, etc. However, foreign ions such as sulfate (SO_4^{2-}), hydroxyl (OH^-) as well as the carbonate ion (CO_3^{2-}) could penetrate from the environment to the pore fluid, then to the surface of the FS. Sulfate ions could inhibit the formation of FS, which also could lead to FS decomposition, during which the bound chloride ions will be released into the pore solution, and form $C_3A \cdot 0.5CaCl_2 \cdot 0.5CaSO_4 \cdot 10H_2O$ (Kuzel's salt).^{16–19} The variation of pH values in the pore fluid would synergistically affect the stability of FS, forming $C_3A \cdot Ca(OH)_2 \cdot nH_2O$ (C_4AH_n).^{9–24} Also, the dissolution of CO_2 could not only change the pH values in the pore fluid, but also cause the FS to be converted into C_4AH_{13} during which the chloride ions would be released, and then the metastable phase C_4AH_{13} would be converted into calcium carbo-aluminate hydrate and ultimately transformed to $CaCO_3$,^{25–27} which causes deterioration of the durability of reinforced concrete. Generally, the ion substitution mechanism in the FS is caused by the replacement of intermediate anions, as is shown in Equations (2)–(5):

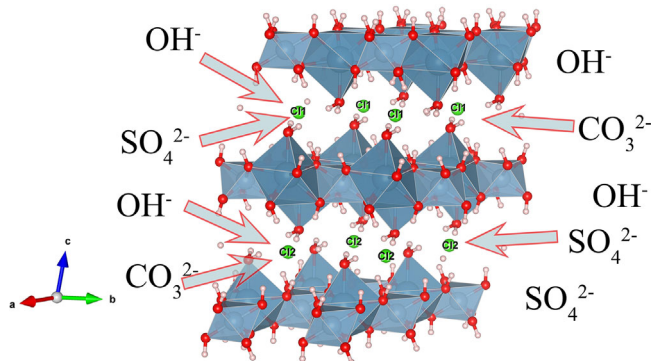
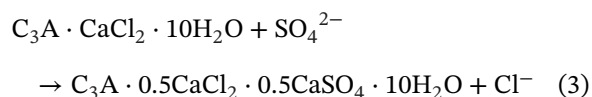
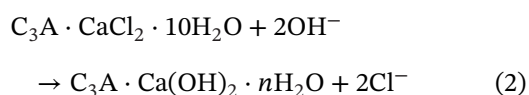


FIGURE 1 Mechanism of chloride ion substitution in the Friedel's salt (FS) crystal by several marine anions

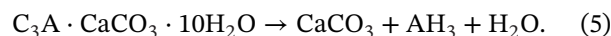
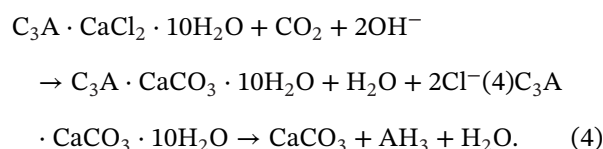


Figure 1 shows the ion substitution mechanism of FS polymorphs. The interlayer chloride ions occupy relatively easily-substitutive sites. Therefore, it is the type of calcium–aluminum oxide polyhedron that determines the stability of the interlayer chloride ions. As shown in Figure 1, the layered-polyhedra have a combination of layered-like aluminum–oxygen tetrahedra and calcium–oxygen octahedra. The FS is formed primarily from a reaction between chloride and aluminum-rich hydration products, such as hydrated calcium aluminate,¹¹ which have the calcium–aluminum oxide polyhedron structure. Once the aluminum is substituted with another element, the distribution of the valence band maximum (VBM) and the distribution of active sites would be changed, possibly resulting in an improved chloride binding stability, preventing the structural chloride from being easily replaced by other ions.²⁸ In other words, stable chloride binding must be chemical binding (where Cl is inside the FS), and its stability depends on the intrinsic electronic structure of the FS.

Thus, modifying FS could lead to improved chloride binding stability. In order to stabilize the chloride ions in FS, some of the composites or atoms (elements) in the layered-polyhedra of FS could be replaced by some inexpensive, earth-abundant, and non-metal elements. However, a direct modification of only the FS is impossible because FS is formed together with the hydrated production. Instead, because FS is formed from the CA hydration process, it is possible to modify the FS precursor, CA. Then, when CA is hydrated, it would form the modified FS.

Along these lines, this study proposes an indirect strategy for modifying FS.

A preliminary list of elements for cement clinker modification, which satisfy criteria including being inexpensive, earth-abundant, and non-metallic, are sulfur, phosphorus, and silicon. Silica can be excluded since modified calcium aluminates clinkers have relatively low hydration activities. Sulfur and phosphorus can be considered since the $[\text{SO}_4]$ tetrahedra and $[\text{PO}_4]$ can be incorporated into the CA lattice under a calcination process to form the stable modified phase.^{29,30} Between the sulfur and phosphorus-based modifiers, the phosphorus-based modifier would be an ideal candidate to modify the calcium aluminates because the hydration products of phosphorus-modified calcium aluminates have a denser and a more intertexture micromorphology than the sulfur-modified one. This is because the ettringite with poor anti-chloride-permeability and later-period volumetric shrinkage properties can be formed in the hydration product of SACs.³¹

In this study, the chloride binding stability of calcium aluminate and P-modified calcium aluminate minerals have been compared. The monocalcium aluminate (CA) was selected as a representative for the calcium aluminate family in this study because it has the highest hydration activity among CA, C_3A , CA_2 , CA_6 , and C_{12}A_7 . The hydration rates of CA_2 are low, typically on the timescale of a week; C_3A and C_{12}A_7 , on the other hand, are too active to control the hydration. CA_6 is regarded as a negligible species in the CAC. CA is the primary mineral phase with controllable and moderate hydration rates in CAC, which can be easily formed when the calcination temperature reaches over 1400°C . In terms of the modification method: given that the phosphorus element doping into the aluminum-rich phase usually forms calcium phosphoaluminate ($\text{C}_8\text{A}_6\text{P}$); meanwhile, the $\text{C}_8\text{A}_6\text{P}$ is the predominant and primary active phase of phosphoaluminate cement (PACs), polycrystalline $\text{C}_8\text{A}_6\text{P}$ powder was directly taken into consideration.

Additionally, combined with state-of-the-art density functional theory (DFT) calculations, it is revealed from the electronic structure why P-modified calcium aluminate has superior chloride binding stability.

2 | MATERIALS AND COMPUTATIONAL DETAILS

2.1 | Samples preparation

2.1.1 | Mineral synthesis

Chemical reagents (CaO , Al_2O_3 , P_2O_5) from Sinopharm Co., Ltd. were used to synthesize calcium phosphoalumi-

nates ($8\text{CaO}\cdot 6\text{Al}_2\text{O}_3\cdot \text{P}_2\text{O}_5$; $\text{C}_8\text{A}_6\text{P}$) and monocalcium aluminate ($\text{CaO}\cdot \text{Al}_2\text{O}_3$; CA) minerals. The raw materials were blended uniformly in water, dried, and pressed into $100 \times 100 \times 1 \text{ mm}^3$ thin film-like sheets by the tablet press machine at 20 MPa. The discs were dried in an oven at 60°C for 48 h to remove the free water. Then, the raw material sheets were sintered at 1400°C (for CA) and 1560°C (for $\text{C}_8\text{A}_6\text{P}$) for 2.5 h and immediately cooled under the atmospheric surroundings. These minerals CA and $\text{C}_8\text{A}_6\text{P}$ were ground with a planetary ball mill and screened with a 0.075 mm sieve. SACs and ordinary Portland cement (OPC) with the type of 42.5 clinkers were obtained from Shan-Shui Cement Co, Ltd. The powder X-ray radiation diffraction (XRD) patterns of raw mineral powder $\text{C}_8\text{A}_6\text{P}$ and CA are shown in Figure 2.

2.1.2 | Sample curing

The raw clinkers were mixed to a water/cement ratio of 0.4. Pastes were placed in $2 \times 2 \times 2 \text{ cm}^3$ molds and then a vibration was applied to them. These hardened pastes cured for 1 day were demolded and transferred to the deionized water curing environment for specific ages. Then, the samples cured for 28 days were immersed into 0.5 and 1 M NaCl solution as the simulated external Cl^- source and terminated their hydration process in required ages, where the Cl^- concentration was set to the typical ocean surroundings and high salinity area. After that, the samples exposed to Cl^- cured for 28 days were then transferred into a carbonation curing oven with the RH of 60% and the CO_2 concentration of 1%. The hydration process of these obtained samples was immediately terminated with anhydrous ethanol.

2.2 | Testing methods

2.2.1 | Chloride binding

The bulk samples, as mentioned above, were crushed and screened to particle sizes ranging from 0.30 to 0.15 mm. These crushed sample particles were placed a conical flask containing 150 ml of deionized water. The conical flask was then left soaking for 1 day after being shaken for 20 min, considering the balance of successive hydration and chloride equilibrium. A total of 100 ml of supernatant was removed from the sample; potassium chromate was used as an indicator, with a nominal concentration of 0.05 M silver nitrate solution to determine the chloride ion content of the solution. Equation (6) was then used to calculate the amount of bound chloride ions in each sample, as shown in Figure 3:

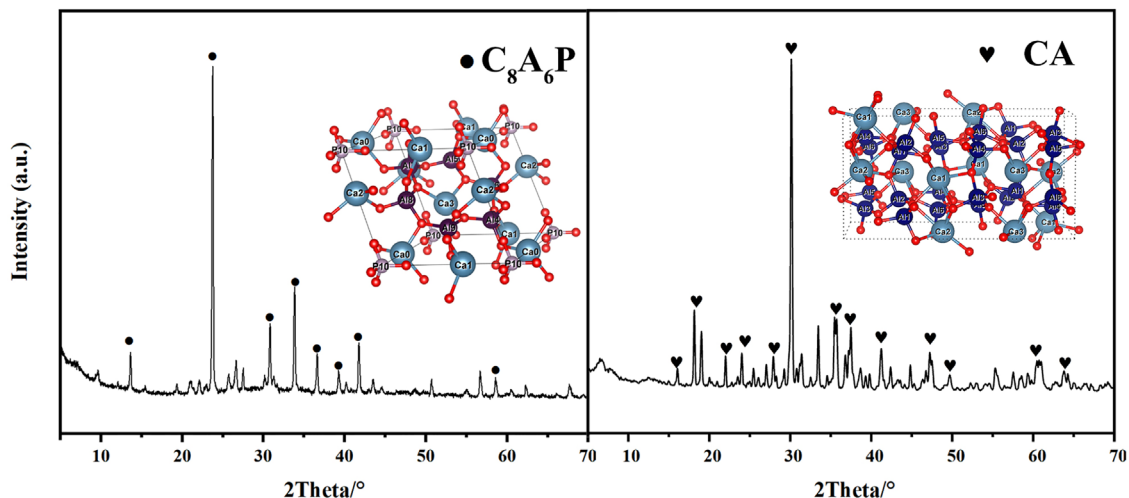


FIGURE 2 X-ray diffraction (XRD) patterns of C_8A_6P and Calcium aluminate (CA) minerals powder and the corresponding primitive cell of the two polymorphs

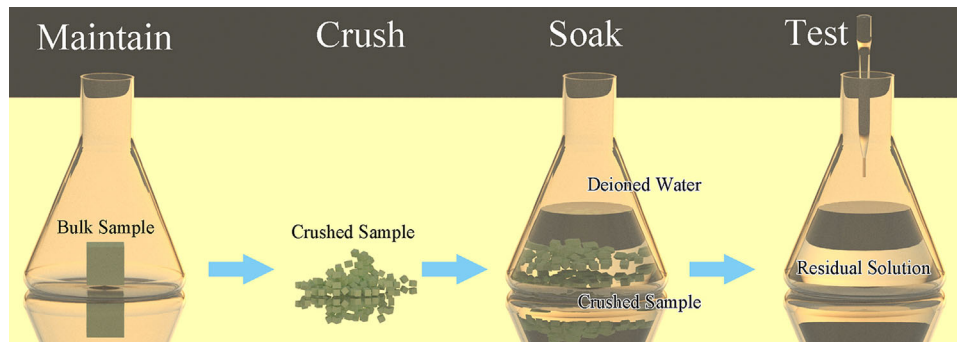


FIGURE 3 Schematic diagram of bound chloride ions determination process

$$C_b = \frac{N_t - (35.453 \times V \times C_f)}{W_d}, \quad (6)$$

where C_b is bound chloride mass mg/g clinkers; N_t is the initial chloride dosage of admixed NaCl in mol; C_f is free chloride concentration at the equilibrium of the external solution in mol/L; V is the volume of the external solution after getting the equilibrium in ml; and W_d is the dry mass of the sample in mg.

2.2.2 | Components and microstructure investigation

Finely ground samples were tested with a Bruker D8 Advanced X-ray diffractometer (with the Cu target source, 40 V, 40 mA). XRD patterns were collected in the range from 5° to 45° with a step angle of 0.02° and a scan speed of 6 deg/s. Derivative thermogravimetric (DTG) analysis was conducted on the finely ground paste samples using

a TGA/DSC/1600HT analyzer heated from 25 to 400°C , with a ramp rate of $5^\circ\text{C}/\text{min}$ under Ar gas. In situ high-temperature X-ray diffraction (In situ-HTXRD) patterns were obtained with a Rigaku SmartLab SE diffractometer (with the Mo target source, 40 V, 40 mA) with an in situ heating mount. The heating temperature was selected from 100 to 500°C , determined by the DTG statistics. Scanning electronic microscopy (SEM) images were obtained from the Quanta FEG 250 and Oxford X-Max-50 energy dispersive spectroscopy (EDS). The EDS mapping signal was collected with over 3500/pc counting rate and exposed more than 120 s per images.

2.3 | Computational details

2.3.1 | Model scheme

FS crystal structure statistics³² were obtained from the inorganic crystal structure database. The primitive cell

TABLE 1 Experimental and calculated lattice parameters for Friedel's salt (FS) and phosphorus-modified Friedel's salt (PFS)

Cell parameters	Experimental						Calculated					
	<i>a</i> (Å)	<i>b</i> (Å)	<i>c</i> (Å)	α (°)	β (°)	γ (°)	<i>a</i> (Å)	<i>b</i> (Å)	<i>c</i> (Å)	α (°)	β (°)	γ (°)
FS	5.665	5.665	15.64	80.56	99.44	121.34	11.64	11.64	16.16	80.67	99.33	121.50
PFS	11.64	11.64	16.16	80.67	99.33	121.50	11.43	11.43	15.27	79.92	100.09	121.56

Note: PFS is 2×2×1 supercell comparing to FS.

was used for static calculation, and a 2 × 2 × 1 supercell was applied to PFS considering the phosphorus-impurities concentration in the real sample. The P element generally replaces the position of Al; the doping site, therefore, was an Al for replacing P with one added O atom coordinated with P for charge compensation in the FS polymorphs.

2.3.2 | Computational parameters

DFT calculations^{33,34} were applied to the two crystal structures calculated using the partial augmented plane wave method³⁵ as implemented in the vienna ab initio simulation package (VASP) code³⁶ with VASPKIT³⁷ for post-processing. Considering that the PFS and FS are layered-like structures, the long-range force correction was considered using the DFT-D3 method of Grimme.³⁸ The Perdew–Burke–Ernzerhof (PBE) generalized gradient approximation³⁹ was used to calculate the exchange-correlation energy with a 400 eV kinetic energy cut-off for the plane-wave basis set. DFT molecular dynamics (MD) simulations were employed for the initial optimization under 300 K with 1 femtosecond (fs)/step lasting for 12.5 ps.

Structural energy minimization was then done using a conjugate gradient method based on the pre-optimized structure until the maximum force component on each atom was below 0.01 eV/Å. The Brillouin zone was sampled with a 5×2×2 Monkhorst–Pack *k*-point mesh.⁴⁰ The local density of states (LDOS) of the VBM and the conduction band minimum (CBM) for FS and PFS were calculated. The electron localization function (ELF) was also calculated to clarify the types of chemical bonds. In order to further explore the contribution of different elements to the band energy closest to the Fermi energy, the total density of states (TDOS) and partial density of states (PDOS) were calculated for Cl and several representative oxygen atoms. Based on the distribution of the LDOS of the VBM on specific atoms, PDOS calculations were performed on specific atoms to explore the contribution of different atoms to the band close to Fermi energy to investigate the active or vulnerable sites of CA and C₈A₆P. The optimized lattice parameters are shown in Table 1. The crystal relative coordinates for FS and PFS are listed in the Supporting Information (SI, Tables S1–S4). The experimental data

for FS were obtained from the Materials Project⁴¹ with the database crystal index of “mp-42175.” The experimental data for PFS were obtained by a Rietveld refinement/fitting from the powder diffraction pattern. The fitting was based upon FS crystallography parameter because the PFS is a derivative of FS.

3 | RESULTS AND DISCUSSIONS

3.1 | Experimental study

Figure 4 depicts the chloride binding capability in CA and C₈A₆P under atmospheric CO₂ environment at different curing ages. Compared with the two graphs (0.5 M and 1 M NaCl environment), the amount of bound chloride ions decreased slightly at the beginning of the curing age of 14 days, indicating that the bound chloride ions play a role in the decomposition. However, from a hydration age of 14–28 days, the bound chloride ions decreased by 46.67% and 46.72% in the 1 M and 0.5 M chloride surroundings for hydration product CA, while only 3.06% and 9.80% bound chloride ions decreased for hydration product C₈A₆P, which shows that the hydration products of C₈A₆P are more stable in chloride binding than the CAs under atmospheric CO₂ environment. In order to understand this chemical reaction mechanism, XRD patterns were plotted to investigate the phase changes during the hydration process under a CO₂ environment. Additionally, the chloride binding stability of SAC and OPC was also investigated, whose results show a relatively low binding capacity and stability.

As shown in Figure 5, without the interference of the chloride ion and without the influence of carbonization, a large amount of CAH₁₀ and C₂AH₈, as well as a small amount of C₃AH₆, were generated in the hydration process of CA as the peak of their XRD patterns shows. When these hydration products were exposed to chloride ions, as shown in the curve of “external Cl⁻ 1d” sample in Figure 5, after one day of exposing to chloride ions, it can be found that the intensity of XRD diffraction peaks corresponding to CAH₁₀ and C₂AH₈ was obviously decreased, while the XRD peak of C₃AH₆'s patterns became obviously increased and more intense; meanwhile, the peak of FS can be initially observed. This indicates that CAH₁₀ and C₂AH₈,

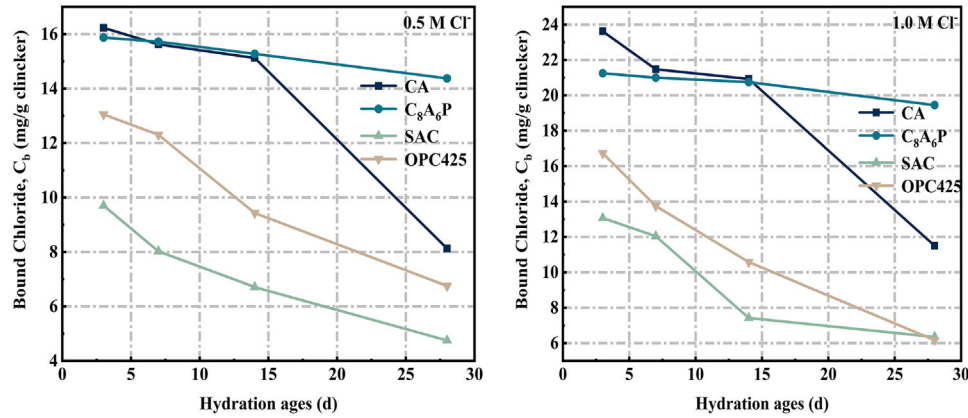


FIGURE 4 Bound chloride of four types of clinkers under different hydration ages in 0.5 M and 1.0 M. NaCl surroundings

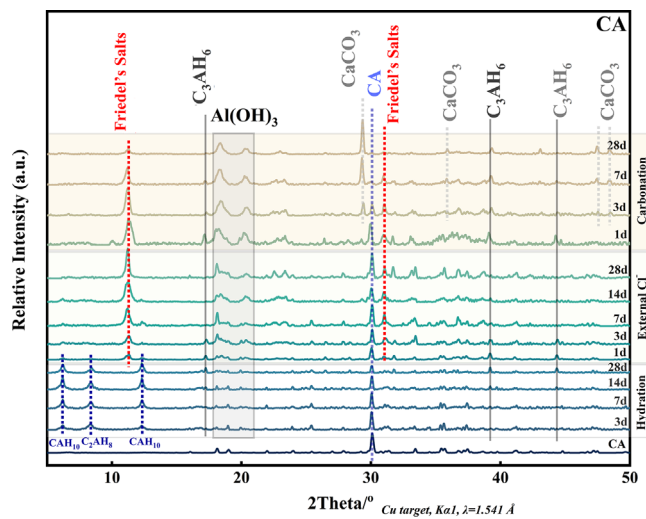


FIGURE 5 PXRD patterns for chloride binding in Calcium aluminate (CA)'s hydration product under hydration ages, external chloride ions immersing and carbonation process

the hydration products of CA, were transformed to the thermodynamically more stable hydration products with a high Ca/Al ratio when they encounter chloride ions, and during this process the chloride ions are effectively immobilized to form FS. With an increase of immersion time of chloride solution for the CA hydration products, it can be seen that the corresponding XRD peak of FS is gradually enhanced, while the peak of C_3AH_6 is clearly weakened, and also the XRD peak of FS is gradually increased, which indicates that there was a transformation from C_3AH_6 to FS in the process of chloride ion binding. Then, all samples were carbonized after soaking in chloride solution for 28 days. The XRD diffraction peak of sample "carbonization 1d" shows that the content of FS remained unchanged after carbonization for 1 day, but the hydration phase C_3AH_6 began to appear. With the increase of exposure time, it can be seen that the peaks of both FS and C_3AH_6 were obvi-

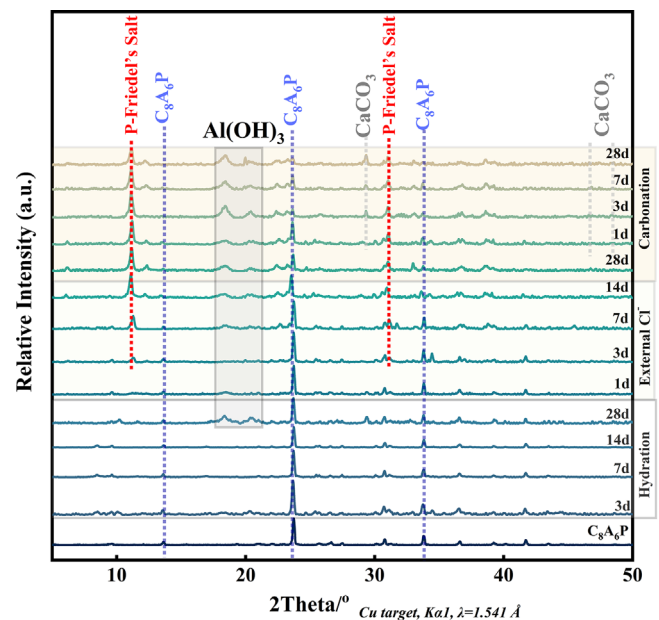


FIGURE 6 PXRD patterns for chloride binding mechanism in C_8A_6P 's hydration product under hydration ages, external chloride ions immersing and carbonation process

ously weakened, and a visible amount of AH_3 and $CaCO_3$ are formed from the relative XRD peak results. From the above, it can be inferred that the peak intensity decreases in the CA group of the FS was attributed to carbonation, which is consistent with previous reports.⁴²⁻⁴⁴

In contrast, Figure 6 shows the XRD diffraction pattern of C_8A_6P after the same treatment. It can be seen that there is no obvious PFS peak on the first day of contact with chloride ions for the 28-days-hydration product, and the visible PFS peak cannot be found until the third day of Cl^- exposure, which indicates that in the early stage, the hydration product of C_8A_6P cannot quickly bind chloride ions. However, with an increase of exposure time in the chloride solution, more PFS were formed. At the same time, the XRD

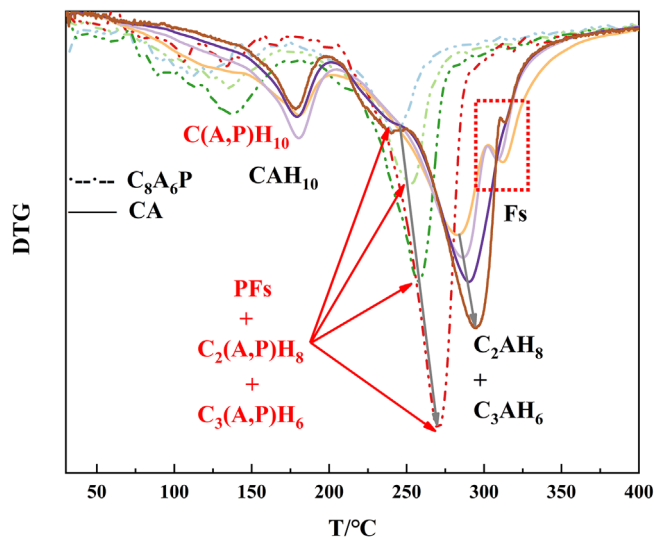


FIGURE 7 Derivative thermogravimetric (DTG) patterns of the hydration production for C_8A_6P and calcium aluminate (CA) at 1 day, 7 days, 14 days, and 28 days in 1 M admixed NaCl. Dotted lines represent the hydration products of C_8A_6P , 1 day (blue), 7 days (shadow green), 14 days (green), and 28 days (red), while straight lines represent the hydration products of calcium aluminate (CA), 1 day (yellow), 7 days (grey), 14 days (purple), 28 days (brown)

peak corresponding to PFS was not weakened significantly after 28 days carbonization, which indicates that the hydration product of C_8A_6P is more stable in facing chloride ions, which explains the results of Figure 4. Consequently, the likely reason for the effective immobilization of chloride ions in the hydration product of C_8A_6P comes from the introduction of phosphorus into the crystal structure of FS.

From the above results, it was justified that good chloride binding stability for C_8A_6P originates from different properties of the FS. However, in wide-angle scanning of XRD patterns it is hard to distinguish the differences between the two types of crystals—FS and PFS. Thus, the DTG pattern of products for the newly found PFS is shown in Figure 7.

Figure 7 shows the DTG curves of CA and C_8A_6P 's hydration products, where the decomposition temperature of CAH_{10} , C_2AH_8 , and C_3AH_6 is higher than phosphorus-doped hydration products $C(A,P)H_{10}$, $C_2(A,P)H_8$, and $C_3(A,P)H_6$ by $\sim 50^\circ\text{C}$. The weight-loss peak at around $300\text{--}325^\circ\text{C}$ is attributed to the dehydration of FS in hydration products of CA,⁴⁵ while much of this kind of weight-loss peaks were not found in hydration products of C_8A_6P , which are left-shifted $\sim 50^\circ\text{C}$, which is the same trend of the other hydration products dehydration temperature and might overlap with the weight-loss peak of $C_2(A,P)H_8$ and $C_3(A,P)H_6$. In order to explain that the weight-loss peak of PFS is overlapped rather than disappeared, it can be seen from Figure 6, which shows the XRD peak of this sample (hydration products of C_8A_6P in 14 and 28 days)

at an angle (2θ) of 11.161° ($d = 7.9340 \text{ \AA}$, corresponding to the main peak of (P)FS). Therefore, the DTG results imply that the PFS is existent, rather than being the original FS.

Additionally, the free chloride ions could be bound by the hydration product. Lower Ca/Al ratios hydration products have the relative low decomposition temperature.²⁸ From Figure 7, the weight-loss peak of the metastable phase CAH_{10} and $C(A,P)H_{10}$ both decreased with the hydration age prolonging (also the increase of carbonation degree), which indicates that the CAH_{10} and $C(A,P)H_{10}$ were decomposed as the curing age increased. And the overlapped weight-loss peaks of $C_2(A,P)H_8$, $C_3(A,P)H_6$ are both shifted to the right with increasing hydration age, in which the weight-loss temperature of $C_3(A,P)H_6$ is $\sim 60^\circ\text{C}$ higher than $C_2(A,P)H_8$. This indicates that the low-calcium type (e.g., $C(A,P)H_{10}$, $C_2(A,P)H_8$) hydration products were converted into the high-calcium type hydration products (e.g., (P)FS, $C_2(A,P)H_8$ and $C_3(A,P)H_6$). As a result of this process, free chloride ions might react with the low Ca/Al hydration products to form the thermodynamically stable phase, (P)FS, which makes the conversion of (P)FS a complex and consecutive process.

The two-phase FS and PFS have a different decomposition temperature as the DTG results (Figure 8) show before, while the XRD patterns (Figure 7) actually could not clearly show the obvious shift of PFS by FS of the diffraction peak of 11.2° (2θ). To further validate the existence of PFS, in situ-HTXRD was applied to observe the two different temperatures of these two phases, as shown in Figure 8. It can be seen that the decomposition temperature of FS is around 287°C , while the decomposition temperature of PFS is higher than FS, reaching 319°C , which shows the two different properties as the different intrinsic decomposition temperature, though, the different crystal structure and properties of the two phases.

For the system of C_8A_6P , a more stable PFS salt may be generated in the hydration process as the previous hypothesis. In order to verify the existence of PFS using another technique, we carefully looked for FS and PFS phases in the hydration products of CA and C_8A_6P that were immersed in the Cl^- solution. In this process, SEM and EDS were employed. As shown in Figure 9, it can be seen that the morphology of FS and PFS grew as a hexagonal thin sheets in the electron microscope images where FS and PFS exist, which is the same as the morphology of FS that has been widely reported previously. In addition, as the EDS results shows, the PFS salt generated by chloride ions encountered in the CA containing phosphorus element contains abundant phosphorus element, confirming the existence of FS containing phosphorus, namely PFS.

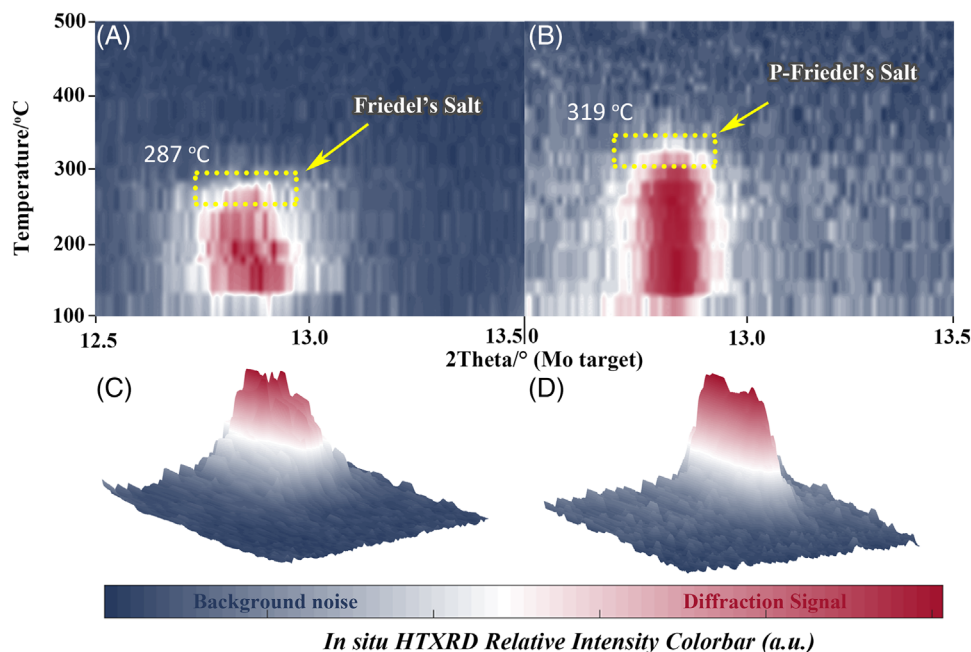


FIGURE 8 In situ high-temperature X-ray diffraction (HTXRD) patterns of Friedel's salt (FS) (001) facet (A) and phosphorus-modified Friedel's salt (PFS) (001) facet (B) and their corresponding three-dimensional (3D) X-ray diffraction (XRD) transform diagram

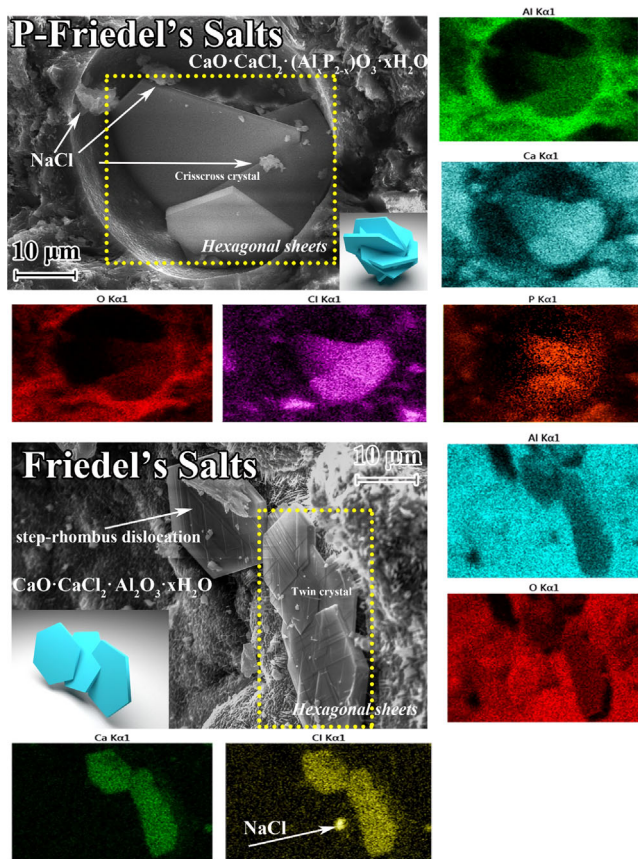


FIGURE 9 Scanning electronic microscopy (SEM) and energy dispersive spectroscopy (EDS) images of Friedel's salt (FS) and phosphorus-modified Friedel's salt (PFS)

3.2 | Density functional theory study

In Section 3.1, it was justified that chloride ions are stable in the hydration products of C₈A₆P. To further understand this, DFT calculations were performed to measure the chemical activity and stability of crystals, as is becoming popular in recent years with increased use of model prediction.^{46–51} In order to provide an explanation that chloride ions can be stably bound in phosphorus-doped samples, widely-employed^{52–55} Fukui function^{56,57} as a reactivity descriptor was used to illustrate the stability in the two bulk PFS and FS, respectively.

The Fukui function is described as Equation (7):

$$f(r) = [(\partial\rho(r)) / (\partial N)]_{v(r)}, \quad (7)$$

where r is the distance in real space, ρ is the electron density, and $N_{v(r)}$ is the number of the electrons under a constant potential field.

The easier the polymorphs are to be ionically attacked, the higher the Fukui function value is. An approximation was defined as $f^-(r) \approx \rho_{\text{HOMO}}(r)$ with respect to electrophilic attack and $f^+(r) \approx \rho_{\text{LUMO}}(r)$ to describe nucleophilic attack. However, in the bulk crystal, the VBM and the CBM are approximately represented as highest occupied molecular orbital (HOMO) and lowest unoccupied molecular orbital (LUMO).⁵⁸ Chemical reactions commonly comprise the excitation of electrons from their LUMO to HOMO. Considering the bulk system, the LDOS

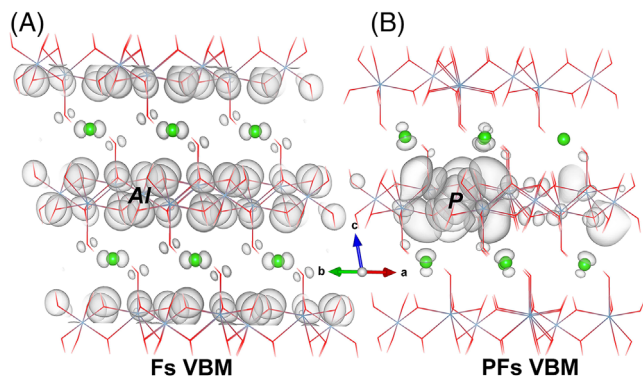


FIGURE 10 LDOS of the valence band maximum (VBM) in real space projection for (A), (B) Friedel's salt (FS) and phosphorus-modified Friedel's salt (PFS). The red vertex represents O, atoms in green represents Cl

of VBM and CBM as the system reactivity information providers were drawn in Figure 10.

The results (Figure 10A) clearly show that the electron density of VBM around the O atoms made the O atoms lose their electrons easier, thus FS are more susceptible to electrophilic attack, while the electron (Figure 10B) that was primarily localized on the impurity P atoms, not on O atoms, where the decrease of electron density on O atoms made O atoms not vulnerable to electrophilic attack by cations. As for Cl atoms, although the distribution of the VBM in PFS (Figure 10B) was localized on the Cl atom, the electron density of VBM was asymmetrically changed compared to that in FS, where the majority of Cl 2p-orbitals had a tendency to interact with the P frontier orbitals of VBM, while some of Cl atoms charged in a low concentration or even lost their electrons. The discrepancy between the two bulk VBM distribution shows that the lower charge density localized on Cl in the PFS makes the localized Cl atoms in PFS resistant to electron loss. Therefore, the PFS is more stable to electrophilic attack. For the lowest CB of the two crystals, as shown in Figure 11, the LDOS of CBMs for FS and PFS were not significantly changed, indicating the introduction of phosphorus primarily affecting the distribution of LDOS for the VBM.

For a deeper understanding of the origin of the intrinsic electronic structures shown in Figures 10 and 11, the TDOS and PDOS for PFS and FS were calculated. As shown in Figure 12, the contributions near the Fermi level primarily come from O atoms both in PFS and FS, where there the peak position closest to the Fermi energy of PDOS in PFS (-0.35 eV) is approximately 0.02 eV lower than that in the FS (-0.33 eV), which explains the different frontier charge difference in Figure 10. The peak position closest to the Fermi level (0 eV calibrated in Figure 13) for Cl atoms in PFS of the PDOS decreases at a lower energy by about 0.21 eV. The significant difference for the most occupied

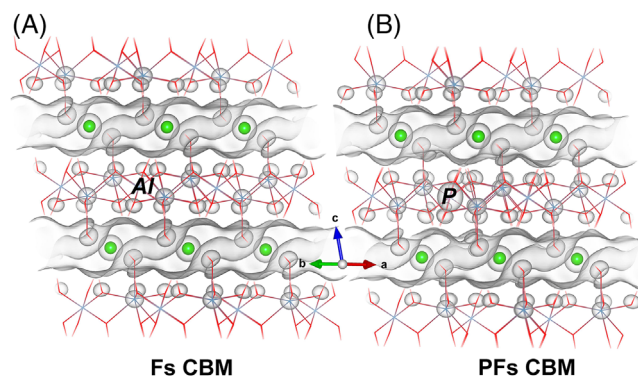


FIGURE 11 LDOS of the conduction band minimum (CBM) in real space projection for (A), (B) Friedel's salt (FS) and phosphorus-modified Friedel's salt (PFS)

energy levels nearest to the Fermi level for Cl can change the chemical activity between the two polymorphs, which indicates that the Cl atom in the FS crystal was more likely to be ionically attacked than that in the PFS.

The peak position of PDOS for O closest to the Fermi level in PFS is slightly lower than the energy in FS because of the difference in the electron distribution of O which directly coordinated with the P atom (Figure 10). In the TDOS (Figure 12) diagram, although the difference between the front orbits in PFS and FS is negligible (0.02 eV), this small difference may come from the difference in the frontier band energy of O coordinated with P, which may significantly affect the stability of the polymorphs. To confirm that this difference is determined by the density of several key O atoms, we calculated and visualized the magnified PDOS diagram for several selected O atoms in the [P–O] pairs (coordinated with P) in PFS, and compared with the PDOS of O atoms in the [Al–O] pairs (coordinated with Al) of the same position in FS. Figure 14 shows three selected and representative O atoms in FS which are coordinated with an Al atom, FS-O9, FS-O10, and FS-O11, which have closer gaps of frontier peaks position to the Fermi level than that in PFS. That is, the peak positions of PDOS for PFS-O32, PFS-O37, and PFS-O42 atoms were left-shifted when compared to those selected atoms in FS, which reveals that P can make the O atoms in the [P–O] pairs less likely to be electrophilic stable.

The change in the chemical reaction activity of the system often depends on the change of the chemical bond in the system, to further investigate the effect of the impurity P element on the electronic structure of FS and PFS, the ELF was calculated and visualized in Figure 15. The ELF depicts a clear separation between the core and valence electron, and also shows covalent bonds and lone pairs,⁵⁹ which is a powerful tool for investigating the nature of the chemical bond and the electron in the neighborhood

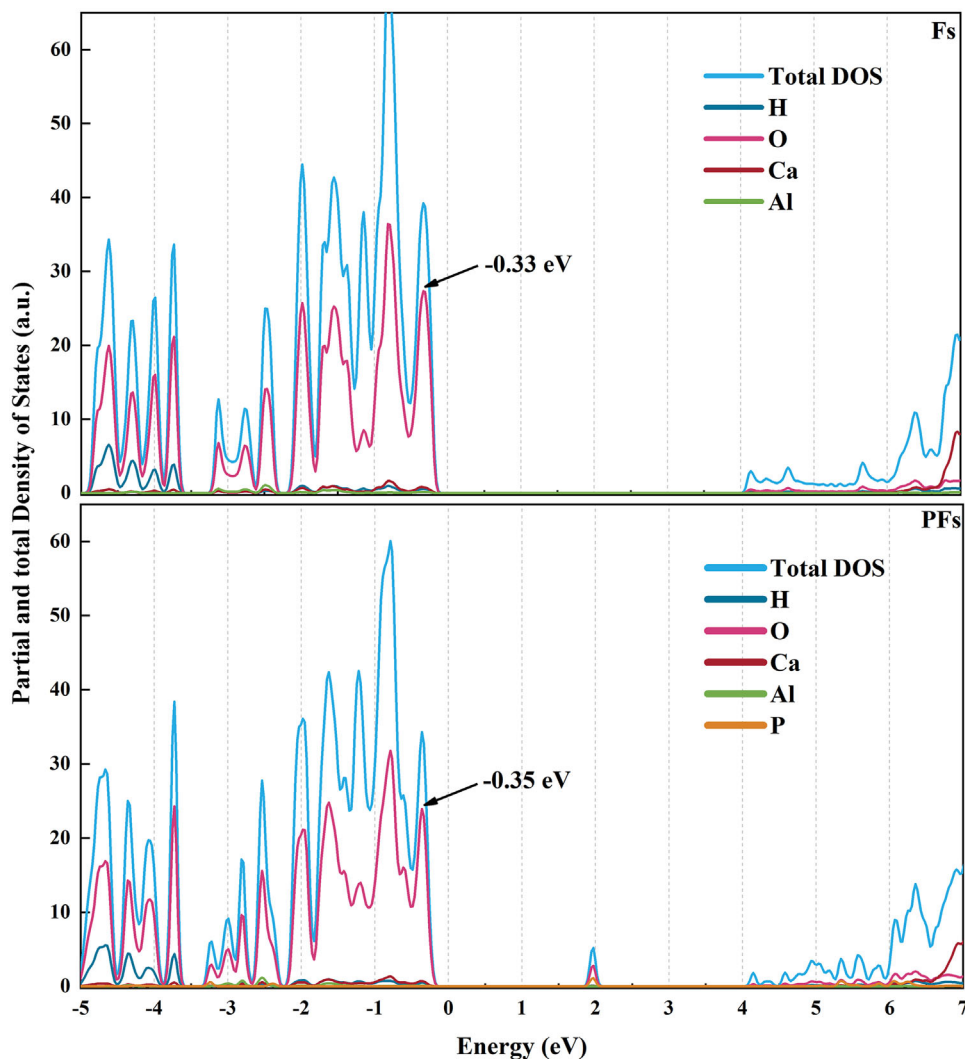


FIGURE 12 Total density of states (TDOS) and partial density of states (PDOS) on each element near the Fermi level. Top: Friedel's salt (FS) ; Bottom: phosphorus-modified Friedel's salt (PFS)

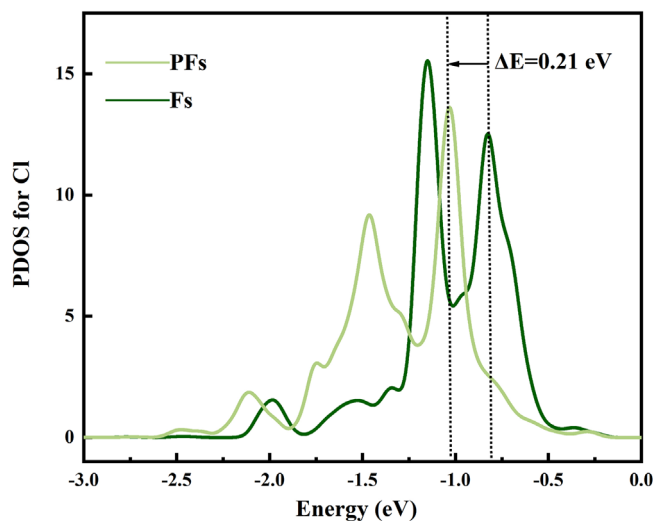


FIGURE 13 Partial density of states (PDOS) projected on Cl of Friedel's salt (FS) and phosphorus-modified Friedel's salt (PFS)

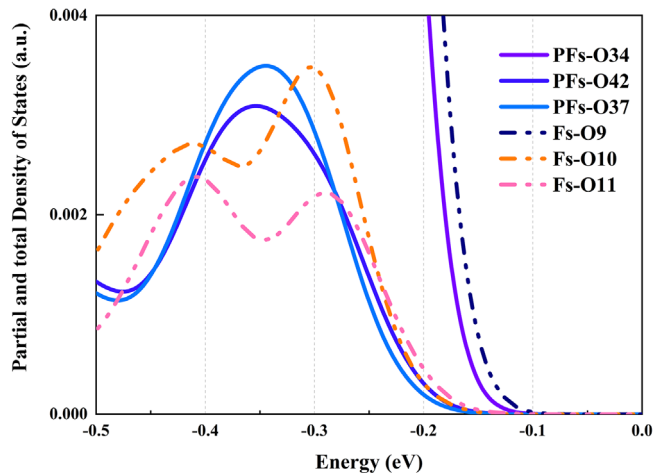


FIGURE 14 Magnified selected atoms partial density of states (PDOS) for O of Friedel's salt (FS) and phosphorus-modified Friedel's salt (PFS). Dash-dotted line: FS; solid line: PFS

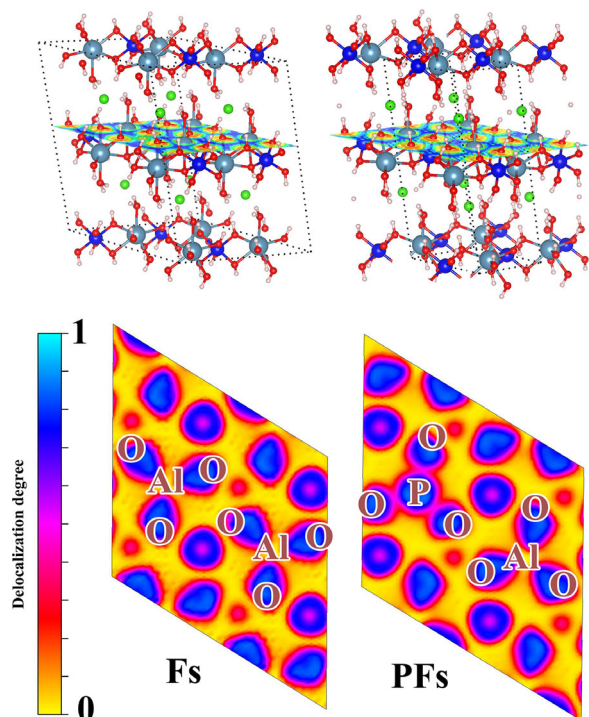


FIGURE 15 Electron localization function (ELF) slice for supercell Friedel's salt (FS) (001.78) and phosphorus-modified Friedel's salt (PFS) (001.78), the top panel is its corresponding slice position in the supercell in real space

space, and it is provided by Equations (8)–(11):

$$D_{\sigma}(r) = \tau_{\sigma}(r) - \frac{1}{4} \frac{(\nabla \rho_{\sigma}(r))^2}{\rho_{\sigma}(r)}, \quad (8)$$

$$D_{\sigma}^0(r) = \frac{3}{5} (6\pi^2)^{2/3} \rho_{\sigma}^{5/3}(r), \quad (9)$$

$$\chi_{\sigma}(r) = \frac{D_{\sigma}(r)}{D_{\sigma}^0(r)}, \quad (10)$$

$$\text{ELF}(r) = \frac{1}{1 + \chi_{\sigma}(r)}, \quad (11)$$

where $D_{\sigma}(r)$ is the contribution due to fermions; $\rho_{\sigma}(r)$ is the electron spin density; $\tau_{\sigma}(r)$ is the kinetic energy density; and $\chi_{\sigma}(r)$ a dimensionless localization index that expresses electron localization for the uniform electron gas.

These ELF (Figure 15) maps reveal the difference in the origin of the chemical bonding differences between FS and PFS. The colder the area in the ELF map, the higher the degree of delocalization of electrons. The same height was chosen for ELF mapping slices in the z -axis direction of FS and PFS, and the slices pass through O atoms directly coordinated with the impurity P atoms. In the PFS ELF slice map, it can be seen that the electrons of the oxygen atom that coordinates with P have delocalized, and significantly interact with the electrons of P, demonstrating the covalent

nature of the P–O bond in PFS. However, the ELF slice map for the Al element in FS that is in the same position in PFS for P does not interact with O obviously, showing certain ionic bond properties. The covalent effect of [P–O] pairs reduce the activity of O atoms, and then lowers the energy of the highest occupied VB, making the selected O atoms PDOS peaks closest to the Fermi energy left-shifted in the P-doped samples, as shown in Figure 14. The peak position closest to the Fermi level of O in one of the [P–O] pairs is lower than that of an [Al–O] pair in FS. Thus, the distinct difference between FS and PFS in the chemical bonding aspect provides a further understanding that the stability of PFs is higher than that of FS.

4 | CONCLUSIONS

In this paper, the chloride binding stability of the hydration product of C_8A_6P and CA pastes were comparatively investigated, and the following conclusions can be drawn:

- The hydration products of C_8A_6P pastes are more stable in chloride binding than hydrated CA pastes under atmospheric CO_2 surroundings.
- The existence of the new mineral PFS in C_8A_6P 's hydration product was justified by the XRD patterns and DTG curves.
- The existence of the newly discovered PFS phase is the main reason for hydration product of C_8A_6P less likely to be carbonated.
- The origin of excellent anti-carbonation nature for PFS was investigated by DFT calculations: the introduction of impurity P element make the VB LDOS electrons localized around P atoms, and lower the VB PDOS peak energy for Cl and O (in the [O–P]) by about 0.21 and 0.05 eV, respectively.
- The reason why the impurity P element can significantly reduce the energy of the VB LDOS of the O atom is P can covalently coordinate with its coordinated O atoms.

Outlook: This article introduces the idea that doped P covalently coordinated with oxygen in FS can significantly improve the chloride binding stability, which provides a guide for the synthesis of materials with high chloride binding stability.

ACKNOWLEDGMENTS

This work was supported by Natural Science Foundation of China (52072149 and 51672108), the Taishan Scholars Program, Case-by-Case partial for Top Outstanding Talents of Jinan. Calculations at the University of Texas at Austin were supported by the Welch Foundation (F-1841).

ORCID

Jia-Ao Wang  <https://orcid.org/0000-0002-4944-4951>

REFERENCES

- Gou M, Guan X. A review of chloride binding in cement-based materials. *Mater Rev*. 2010;24(6):124–7.
- Xu J, Feng W, Jiang L, Xu Y, Song Y, Cao Y, et al. Influence of surfactants on chloride binding in cement paste. *Constr Build Mater*. 2016;125:369–74.
- Bao JW, Li SG, Zhang P, Ding X, Xue S, Cui Y, et al. Influence of the incorporation of recycled coarse aggregate on water absorption and chloride penetration into concrete. *Constr Build Mater*. 2020;239:117845.
- Yang XJ, Liu JS, Li HX, Ren Q. Performance and ITZ of pervious concrete modified by vinyl acetate and ethylene copolymer dispersible powder. *Constr Build Mater*. 2020;235:117532.
- Zibara H. Binding of external chlorides by cement pastes. University of Toronto; 2001.
- Kayali O, Khan MSH, Ahmed SM. The role of hydrotalcite in chloride binding and corrosion protection in concretes with ground granulated blast furnace slag. *Cem Concr Compos*. 2012;34(8):936–45.
- Lee NK, Lee HK. Influence of the slag content on the chloride and sulfuric acid resistances of alkali-activated fly ash/slag paste. *Cem Concr Compos*. 2016;72:168–79.
- Majumdar AJ, Edmonds RN, Singh B. Hydration of Secar 71 aluminous cement in presence of granulated blast furnace slag. *Cem Concr Res*. 1990;111:7–14.
- Shi Z, Geiker MR, De Weerd K, Østnor TA, Lothenbach B, Winnefeld F, et al. Role of calcium on chloride binding in hydrated Portland cement–metakaolin–limestone blends. *Cem Concr Res*. 2017;95:205–16.
- Wang Y, Shui Z, Huang Y, Sun T, Duan P. Properties of coral waste-based mortar incorporating metakaolin: Part II. Chloride migration and binding behaviors. *Constr Build Mater*. 2018;174:433–42.
- Friedel PM. Sur un chloro-aluminate de calcium hydrate sé maclantpar compression. *Bull Soc Fr Mineral*. 1897;19:122–36.
- Renaudin G, Kubel F, Rivera J-P, Francois M. Structural phase transition and high temperature phase structure of Friedel's salt, $3\text{CaO}\cdot\text{Al}_2\text{O}_3\cdot\text{CaCl}_2\cdot 10\text{H}_2\text{O}$. *Cem Concr Res*. 1999;29:1937–42.
- Terzis A, Filippakis S, Kuzel HJ, Burzlaff H. The crystal structure of $\text{Ca}_2\text{Al}(\text{OH})_6\text{Cl}_2\cdot 10\text{H}_2\text{O}$. *Zeit Krist*. 1987;181:29–34.
- Rapin J-P, Noor NM, François M. The double-layered hydroxide $3\text{CaO}\cdot\text{Al}_2\text{O}_3\cdot\text{CaBr}_2\cdot 10\text{H}_2\text{O}$. *Acta Crystallogr. Section C*. 1999;55(8):IUC9900092.
- Xu Y. The influence of sulphates on chloride binding and pore solution chemistry. *Cem Concr Res*. 1997;27(12):1841–50.
- Luo R, Cai Y, Wang C, Huang X. Study of chloride binding and diffusion in GGBS concrete. *Cem Concr Res*. 2003;33(1):1–7.
- Guerrero A, Goñi S, Allegro VR. Effect of temperature on the durability of class C flyash belite cement in simulated radioactive liquid waste: Synergy of chloride and sulphate ions. *J Hazard Mater*. 2009;165(1–3):903–8.
- Al-Amoudi OSB, Maslehuddin M, Abdul-Al YAB. Role of chloride ions on expansion and strength reduction in plain and blended cements in sulfate environment. *Constr Build Mater*. 1995;9(1):25–33.
- Maraghechi H, Avet F, Wong H, Kamyab H, Scrivener K. Performance of limestone calcined clay cement (LC3) with various kaolinite contents with respect to chloride transport. *Mater Struct*. 2018;51:125.
- De Weerd K, Colombo A, Coppola L, Justnes H, Geiker MR. Impact of the associated cation on chloride binding of Portland cement paste. *Cem Concr Res*. 2015;68:196–202.
- Chang J, Xiong C, Zhang Y, Wang D. Foaming characteristics and microstructure of aerated steel slag block prepared by accelerated carbonation. *Constr Build Mater*. 2019;209:222–233.
- Avet F, Scrivener K. Influence of pH on the chloride binding capacity of limestone calcined clay cements (LC3). *Cem Concr Res*. 2020;131:106031.
- Suryavanshi AK, Swamy RN. Stability of Friedel's salt in carbonated concrete structural elements. *Cem Concr Res*. 1996;26:729–41.
- Wang Y, Nanukuttan S, Bai Y, Basheer PAM. Influence of combined carbonation and chloride ingress regimes on rate of ingress and redistribution of chlorides in concretes. *Constr Build Mater*. 2017;140:173–83.
- Delnavaz A, Ramezani-pour AA. The assessment of carbonation effect on chloride diffusion in concrete based on artificial neural network model. *Mag Concr Res*. 2012;64(10):877–84.
- Jin ZQ, Sun W, Li QY. Effect of carbonation on chloride diffusion in concrete. *J Univ Sci Technol Beijing*. 2008;30(8):921–5.
- Parr RG, Yang W. Density functional theory of atoms and molecules. Oxford University Press: New York; 1989.
- Xu Q, Ji T, Yang Z, Ye Y. Steel rebar corrosion in artificial reef concrete with sulfoaluminate cement, sea water and marine sand. *Constr Build Mater*. 2019;227:116685.
- Liu P, Chen Y, Yu Z, Ding Z, Xing F, Lu Z, et al. Early hydration properties and performance evolution of phosphoaluminate cement concrete. *Constr Build Mater*. 2020;233:117318.
- Li J, Li S, Hu J, Liu B, Wang Q. Study on the aluminophosphate glass-rich cement. *Cem Concr Res*. 2001;31:949–52.
- Wang J, Chen Z, Wu K. Properties of calcium sulfoaluminate cement made ultra-high performance concrete: Tensile performance, acoustic emission monitoring of damage evolution and microstructure. *Constr Build Mater*. 2019;208:767–79.
- Renaudin G, Kubel F, Rivera J-P, Francois M. Structural phase transition and high-temperature phase structure of Friedel's salt. *Cem Concr Res*. 1999;29:1937–42.
- Hohenberg P, Kohn W. Inhomogeneous Electron Gas. *Phys Rev*. 1964;155:B864.
- Kohn W, Sham LJ. Self-consistent equations including exchange and correlation effects. *Phys Rev*. 1965;140:A1133.
- Bloch PE. Projector augmented-wave method. *Phys Rev B*. 1994;50:17953.
- Kresse G, Hafner J. Ab-initio molecular dynamics for liquid metals. *Phys Rev B*. 1993;47:558.
- Wang V, Xu N, Liu J, Tang G, Geng W. VASPKIT: A pre- and post-processing program for VASP code. Cornell University; 2019
- Grimme S, Ehrlich S, Goerigk L. Effect of the damping function in dispersion corrected density functional theory. *J Comput Chem*. 2011;32:1456–65.
- Perdew J, Burke K, Ernzerhof M. Generalized gradient approximation made simple. *Phys Rev Lett*. 1996;77:3865.

40. Monkhorst HJ, Pack JD. Special points for Brillouin-zone integrations. *Phys Rev B*. 1976;13:5188.
41. Jain A, Ong SP, Hautier G, Chen W, Richards WD, Dacek S, et al. The materials project: A materials genome approach to accelerating materials innovation. *APL Mater*. 2013;1(1):011002.
42. Wang Y, Nanukuttan S, Baic Y, Basheer PAM. Influence of combined carbonation and chloride ingress regimes on rate of ingress and redistribution of chlorides in concretes. *Constr Build Mater*. 2017;140:173–183.
43. Liu W, Cui H, Dong Z, Xing F, Zhang H, Lo TY. Carbonation of concrete made with dredged marine sand and its effect on chloride binding. *Constr Build Mater*. 2016;120:1–9.
44. Chang H. Chloride binding capacity of pastes influenced by carbonation under three conditions. *Cem Concr Compos*. 2017;84:1–9.
45. Shi Z, Geiker MR, Lothenbach B, De Weerd K, Garzón SF, Enemark-Rasmussen K, et al. Friedel's salt profiles from thermogravimetric analysis and thermodynamic modelling of Portland cement-based mortars exposed to sodium chloride solution. *Cem Concr Compos*. 2017;78:73–83.
46. Tao Y, Zhang W, Shang D, Xia Z, Li N, Ching WY, et al. Comprehending the occupying preference of manganese substitution in crystalline cement clinker phases: A theoretical study. *Cem Concr Res*. 2018;109:19–29
47. Wang Q, Li F, Shen X, Shi W, Li X, Guo Y, et al. Relation between reactivity and electronic structure for α' -L-, β - and γ -dicalcium silicate: A first-principles study. *Cem Concr Res*. 2014;57:28–32
48. Sabziparvar AM, Hosseini E, Chiniforush V, Korayem AH. Barriers to achieving highly dispersed graphene oxide in cementitious composites: An experimental and computational study. *Constr Build Mater*. 2019;199:269–78
49. Asaldoust S, Hosseini MS, Ramezanzadeh B, Bahlakeh G. Construction of a unique anti-corrosion nanocomposite based on graphene oxide@Zn3PO4/epoxy; experimental characterization and detailed-theoretical quantum mechanics (QM) investigations. *Constr Build Mater*. 2020;256:119439
50. Svenum I, Ringdalen IG, Bleken FL, Friis J, Höche D, Swang O. Structure, hydration, and chloride ingress in C–S–H: Insight from DFT calculations. *Cem Concr Res*. 2020;129:105965
51. Scholtzová E, Tunega D, Speziale S. Mechanical properties of ettringite and thaumasite—DFT and experimental study. *Cem Concr Res*. 2015;77:9–15.
52. Cardenas C, Proft FD, Chamorro E, Fuentealba P, Geerlings P. Theoretical study of the surface reactivity of alkaline earth oxides: Local density of states evaluation of the local softness. *Chem Phys*. 2008;128:034708.
53. Geerlings P, De Proft F, Langenaeker W. Chem. conceptual density functional theory. *Chem Rev*. 2003;103:1793.
54. Santos JC, Chamorro E, Contreras R, Fuentealba P. Local reactivity index as descriptor of benzene adsorption in cluster models of exchanged zeolite-Y. *Chem Phys Lett*. 2004;383:612.
55. Manzano H, Dolado JS, Ayuela AJ. Structural, mechanical, and reactivity properties of tricalcium aluminate using first principles calculations. *J Am Ceram Soc*. 2009;92:897.
56. Holton J, Lappert MF, Pearce R, Yarrow PIW. Bridged hydrocarbyl or hydrocarbon binuclear transition metal complexes: Classification, structures, and chemistry. *Chem Rev*. 1983;83:135.
57. Parr RG, Yang W. Density functional approach to the frontier-electron theory of chemical reactivity. *J Am Chem Soc*. 1984;106:4049.
58. Chattaraj PK. Chemical reactivity theory: A density functional view. CRC Press: Boca Raton, FL; 2009.
59. Becke AD, Edgecombe KE. A simple measure of electron localization in atomic and molecular systems. *J Chem Phys*. 1990;92(9):5397–403.

SUPPORTING INFORMATION

Additional supporting information may be found in the online version of the article at the publisher's website.

How to cite this article: Wang JA, Wang S, Henkelman G. Improved chloride binding stability for hydration products of calcium aluminates by phosphorus modification. *J Am Ceram Soc*. 2022;105:4870–4882.
<https://doi.org/10.1111/jace.18441>